Tin Phosphide as a Promising Anode Material for Na-Ion Batteries

Youngjin Kim, Yongil Kim, Aram Choi, Sangwon Woo, Duckgyun Mok, Nam-Soon Choi, Yoon Seok Jung, Ji Heon Ryu, Seung M. Oh,* and Kyu Tae Lee*

Na-ion batteries have recently attracted a great deal of attention as a next-generation battery, because Na resources are inexhaustible and cheaper than Li resources. However, although Na-ion batteries have shown promising electrochemical performance including stable cycleability and good rate capability, it should be stressed that it is not easy for Na-ion batteries to replace Li-ion batteries owing to the critical issue of Na-ion batteries having slightly lower energy density than Li-ion batteries.[1–6] The lower energy density of Na-ion batteries is attributed to the lower specific capacity and redox potential of most Na-ion insertion materials that have been introduced to date. Therefore, in order to successfully replace Li-ion batteries by Na-ion batteries, new negative electrode (anode) materials having a high specific capacity and low redox potential should be introduced. Recently, there have been a few studies on Na-ion insertion materials for use in anodes with a high specific capacity. For examples, Sn[7–11]- and Sb[12–17]-based materials have been examined as promising anode materials, and they delivered a high reversible capacity of approximately 500~700 mA h g^{-1}. While Sb-based materials exhibited stable cycle performance, Sn-based materials showed poor reversibility. However, the redox potential of Sn is lower than that of Sb, and thus, Sn-based materials are more beneficial for obtaining higher energy density (working voltage). Also, phosphorus/carbon composite materials have shown excellent electrochemical performance including the highest specific capacity (1890 mA h g^{-1}) among all reported anode materials.[18,19] However, phosphorus has poor electrical conductivity, and thus, a large amount of carbon (~30 wt.%) has to be used in the phosphorus/carbon composites to enhance their electrical conductivity, which decreases their gravimetric and volumetric energy densities. The

volumetric energy density of a battery is one of the most critical factors that determine its suitability as a next generation battery for use in electric vehicles and mobile devices. Therefore, it is important to develop new electrode materials delivering high volumetric specific capacity for Na-ion batteries. In this study, Sn_4P_3 was examined for the first time as an anode material for Na-ion batteries. The theoretical volumetric capacity of Sn_4P_3 is 6650 mA h cm^{-3}, which is much higher than that of a phosphorus/carbon (7:3 wt. ratio) composite (2431 mA h cm^{-3}) and even higher than that for bare phosphorus (5710 mA h cm^{-3}), as shown in **Figure 1**a. This volumetric capacity of Sn_4P_3 is the highest among Na-ion insertion materials reported to date. Figure 1b also represents the gravimetric and volumetric energy densities for full cells composed of various anode materials and the cathode material of P2-Na$_{2/3}$[Fe$_{1/2}$Mn$_{1/2}$]O$_2$.[15] The other details of calculation parameters including material densities, working voltage, specific capacities, electrode porosity, and the thickness of current collectors are given in Table S1. Moreover, the electrical conductivity of Sn_4P_3 is 30.7 S cm^{-1}, which is much higher than that of a phosphorus/carbon (7:3 wt. ratio) composite (3.5 × 10^{-5} S cm^{-1}).[18] Accordingly, carbon-containing composites can be dispensed with Sn_4P_3. It was previously thought that Sn_4P_3 was not a promising anode material for Li-ion batteries because of its poor cycle performance and relatively high redox potential as an anode. Thus, only a few studies have focused on the just lithiation and delithiation reaction mechanism of Sn_4P_3,[20,21] although various metal phosphide materials have been extensively studied for use in Li-ion batteries.[22–31] However, in this study, Sn_4P_3 as an anode for Na-ion batteries shows excellent electrochemical performance. Sn_4P_3 delivered a high reversible capacity of 718 mA h g^{-1}, and showed very stable cycle performance with negligible capacity fading over 100 cycles; the cycle performance of Sn_4P_3 was better than those of previously reported Sn-based materials and phosphorus/carbon composites.[8–11,18,19] Moreover, Sn_4P_3 delivered its reversible capacity at an appropriately low redox potential of about 0.3 V vs. Na/Na$^+$. The redox potential of Sn_4P_3 is lower than that of phosphorus, indicating that the energy density of a full cell with a Sn_4P_3 anode would be higher than that of a full cell with a phosphorus anode when assumed that both anode materials deliver equal reversible capacities.

An intermetallic compound of Sn_4P_3 was obtained by facile high-energy mechanical ball milling in an Ar atmosphere for an hour. Figure 1c shows the X-ray diffraction (XRD) pattern and the corresponding Rietveld refinement of as-prepared Sn_4P_3 powders, and no impurity was observed. The lattice parameter and agreement factors of Sn_4P_3 powders obtained

Y. Kim, Prof. S. M. Oh
School of Chemical and Biological Engineering
Seoul National University
599 Gwanangno, Gwanak-gu, Seoul
151–744, South Korea
E-mail: seungoh@snu.ac.kr
Y. Kim, A. Choi, S. Woo, D. Mok, Prof. N.-S. Choi,
Prof. Y. S. Jung, Prof. K. T. Lee
School of Energy and Chemical Engineering
Ulsan National Institute of Science and Technology (UNIST)
100 Banyeon-ri, Eonyang-eup, Ulju-gun, Ulsan 689–798, South Korea
E-mail: ktlee@unist.ac.kr
Prof. J. H. Ryu
Graduate School of Knowledge-based Technology and Energy
Korea Polytechnic University
Gyeonggi 429–793, South Korea
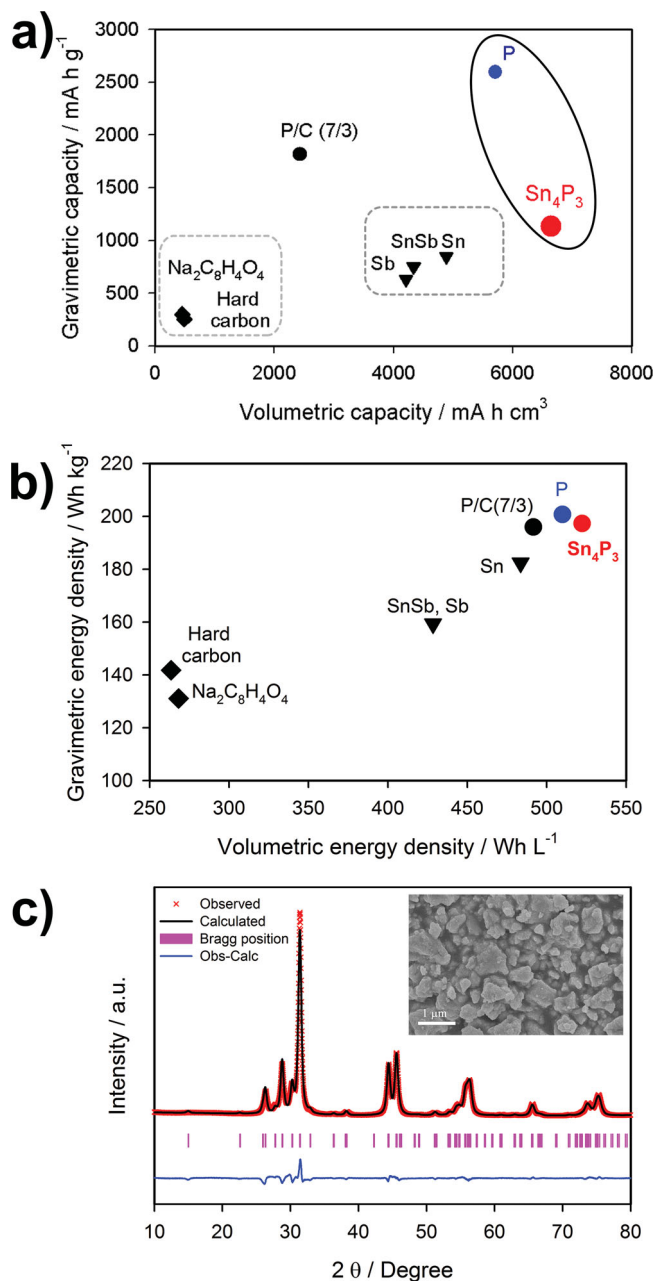
COMMUNICATION

Figure 1. (a) Theoretical volumetric and gravimetric capacities for various anode materials in Na-ion batteries. (b) Theoretical volumetric and gravimetric energy densities for full cells with various anode materials. (c) X-ray diffraction pattern and the corresponding Rietveld refinement of Sn_4P_3 (inset: FE-SEM image)

from Rietveld refinement is given in Table S2. The space group of the Sn_4P_3 crystal structure is *R-3m*, and Sn_4P_3 crystallizes in a rhombohedral lattice.[20] The electrochemical performance of the Sn_4P_3 electrode was evaluated using a half cell with a sodium counter electrode. **Figure 2** shows a comparison of the cycle performance and voltage profiles of Sn and Sn_4P_3. Both electrodes delivered a similar reversible capacity of about 718 mA h g^{-1} when an fluoroethylene carbonate (FEC) additive was used, but Sn_4P_3 showed much more improved cycle

performance than Sn, as shown in Figure 2a. Moreover, Sn_4P_3 exhibited negligible capacity fading over 100 cycles in spite of its larger micrometer-sized particles (the inset of Figure 1c) than nanosized Sn particles (Figure S1). Without the FEC additive, Sn_4P_3 delivered a higher reversible capacity of about 833 mA h g^{-1}, but showed worse cycle performance. As is well known, this indicates that the FEC additive forms stable SEI layers, resulting in excellent cycle performance of Sn_4P_3. However, NaF-like SEI layers obtained from the FEC additive increases a charge-transfer resistance, causing an increase of polarization, and this results in a lower reversible capacity.[11,17,19] This is consistent with the differential capacity (dQ/dV) plots of Sn_4P_3 with or without the FEC, and Sn_4P_3 with the FEC showed smaller polarization than that without the FEC (Figure 2e). Figures 2b–d show the charge-discharge profiles of the Sn_4P_3 with or without the FEC and Sn with the FEC, respectively, between 1.5 and 0 V vs. Na/Na$^+$ at a rate of 100 mA g^{-1} (~0.15C). The sodiation profile of Sn_4P_3 shows two steps located at ~0.2 and 0.01 V vs. Na/Na$^+$, which is further supported by differential capacity (dQ/dV) plots (Figure 2e) and the quasi-open-circuit-voltage (QOCV) profile (Figure S2) obtained via the galvanostatic intermittent titration technique. The plateau at ca. 0.2 V was attributed to the formation of Na_xP and NaSn phases via a conversion reaction, and further sodiation occured at ca. 0.01 V to form $Na_{15}Sn_4$. This sodiation mechanism was supported by ex situ HR-TEM analysis and fast Fourier transformation (FFT) studies. **Figures 3**a and 3b show the voltage profile of the Sn_4P_3 without the FEC and the corresponding HR-TEM images with FFTs (inset: right) of the selected area (inset: left) at various degrees of sodiation, respectively. The initial state before sodiation is Sn_4P_3, which is consistent with that the d-spacings obtained from FFT analysis corresponded to (110) and (107) of Sn_4P_3 (Figure 3b (i)). This is further supported by the selected area electron diffraction (SAED) pattern of the initial state, as shown in Figure 3c (i). As the redox potential reached at 0.07 V vs. Na/Na$^+$, NaSn nanocrystallites (dark region) with sizes of tens of nanometers dispersed in an amorphous Na_xP matrix (bright region) were observed. As shown in the insets of Figure 3b (ii), the d-spacings of the crystalline nano-domains dispersed in the amorphous matrix measured from FFT analysis corresponded to (402) and (215) of NaSn. This reveals that NaSn was formed via the conversion reaction accompanying the formation of amorphous Na_xP. The formation of NaSn nanocrystallites was further supported by energy dispersive X-ray spectroscopy (EDS) line profiles shown in Figure 3d. The intensity of Sn increased in the nanocrystalline (bright) region, and the intensity of Na in the nanocrystalline region was similar to that in the amorphous (dark) region corresponding to Na_xP. This implies that Na was inserted not only in the amorphous phosphorus matrix but also in the Sn nanocrystallites. At point (iii) after full sodiation, larger nanocrystallites dispersed in the amorphous matrix were observed (Figure 3b (iii)). The d-spacings of the crystalline nano-domains dispersed in the matrix measured from FFT analysis corresponded to (332) and (310) of $Na_{15}Sn_4$, indicating that NaSn was further sodiated to form $Na_{15}Sn_4$ at ca. 0.01 V. The larger size of the nanocrystallites shown in (iii) further supported the formation of $Na_{15}Sn_4$ (22.3 ± 1.1 nm), because the increase in the nanocrystallite size was attributed to the

Materials
Views
www.MaterialsViews.com

ADVANCED
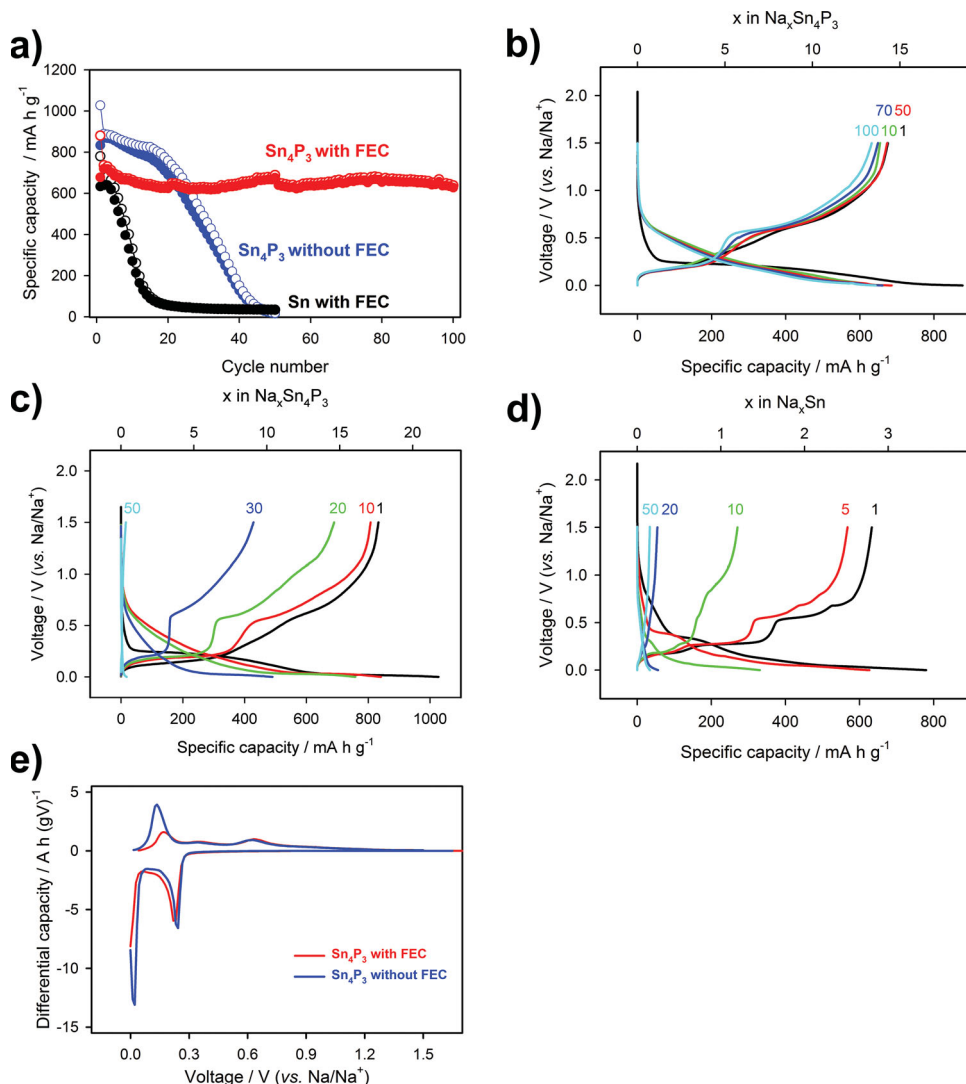MATERIALS
www.advmat.de

COMMUNICATION

Figure 2. (a) Cycle performance of Sn_4P_3 and Sn electrodes obtained with or without an FEC additive, and the corresponding voltage profiles of (b) Sn_4P_3 with an FEC additive, (c) Sn_4P_3 without an FEC additive and (d) Sn with an FEC additive. (e) Differential capacity (dQ/dV) plots of Sn_4P_3 electrodes for the first cycle with or without an FEC additive.

bution function of the EXAFS signals for Sn_4P_3 at selected degrees of sodiation from (i) to (iii). For the pristine electrode, a distinct peak at 2.178 Å corresponding to the Sn-P bond was observed, while the peak corresponding to the Sn-P bond decreased and a new peak corresponding to the Sn-Sn bond appeared at 0.07V (ii). After full sodiation (iii), FT peaks corresponding to the Sn-P bond is notably decreased, indicating that the Sn-P bond cleaved and long range order decreased because of amorphization, as Na ions were inserted in the Sn_4P_3 structure.

In order to further clarify the structural changes upon sodiation/desodiation, ex situ XRD analysis of Sn_4P_3 was performed, and it revealed that the reversible sodiation/desodiation of Sn_4P_3 proceeded in a two-phase reaction, as shown in **Figure 4**. Upon sodiation to 0.07 V, the intensity of XRD peaks corresponding to Sn_4P_3 decreased, but no new peaks were observed despite the fact that crystalline NaSn and $Na_{15}Sn_4$ nanodomains were observed in the TEM images. This indicates that an amorphous Na_xP phase was formed during sodiation and nanocrystalline NaSn was not detectable by XRD owing to its very small crystallite size. After full sodiation, very broad peaks corresponding to sodiated Sn phases

volume expansion from NaSn (15.1 ± 0.4 nm). In addition, it was considered that this morphology of the confinement of Na_ySn nanocrystallites in the amorphous Na_xP matrix made a critical contribution toward the better cycle performance of Sn_4P_3 than Sn. It is well-known that the pulverization or cracking of Sn is caused by the agglomeration of Sn particles during cyclings in Li-ion batteries, resulting in the degradation of Sn electrodes. However, in the case of Sn_4P_3, Sn nanocrystallites are embedded in the phosphorus matrix during cyclings, and thus the agglomeration of Sn is inhibited.

The sodiation mechanism of Sn_4P_3 is consistent with extended X-ray absorption fine structure (EXAFS) data shown in Figure 3e. X-ray absorption spectroscopy (XAS) was carried out on Sn atoms in the active electrode materials to observe the evolution of local structural variations during Na insertion. Figure 3e displays the Fourier transform $k^3\chi(k)$ radial distri-

such as $Na_{15}Sn_4$ and Na_9Sn_4 appeared at ~19 and 33°, as shown in the enlarged XRD patterns (Figure 4b). This observations agreed well with the ex situ TEM result (Figure 3). On desodiation, the intensity of XRD peaks corresponding to Sn_4P_3 gradually increased, indicating that the conversion reaction of Sn_4P_3 to Na_xP and $Na_{15}Sn_4$ was reversible. This observation was consistent with the TEM studies of the fully desodiated phase converted from the mixed phases of Na_xP and $Na_{15}Sn_4$, as shown in Figures 3b and 3c (iv). The embedded NaSn and $Na_{15}Sn_4$ nanocrystallites in the matrix disappeared after desodiation and formed Sn_4P_3. This is supported by that the d-spacings obtained from FFT analysis corresponded to Sn_4P_3 (Figure 3b (iv)). Also, this is consistent with the selected area electron diffraction (SAED) pattern after full desodiation corresponding to Sn_4P_3, as shown in Figure 3c (iv).
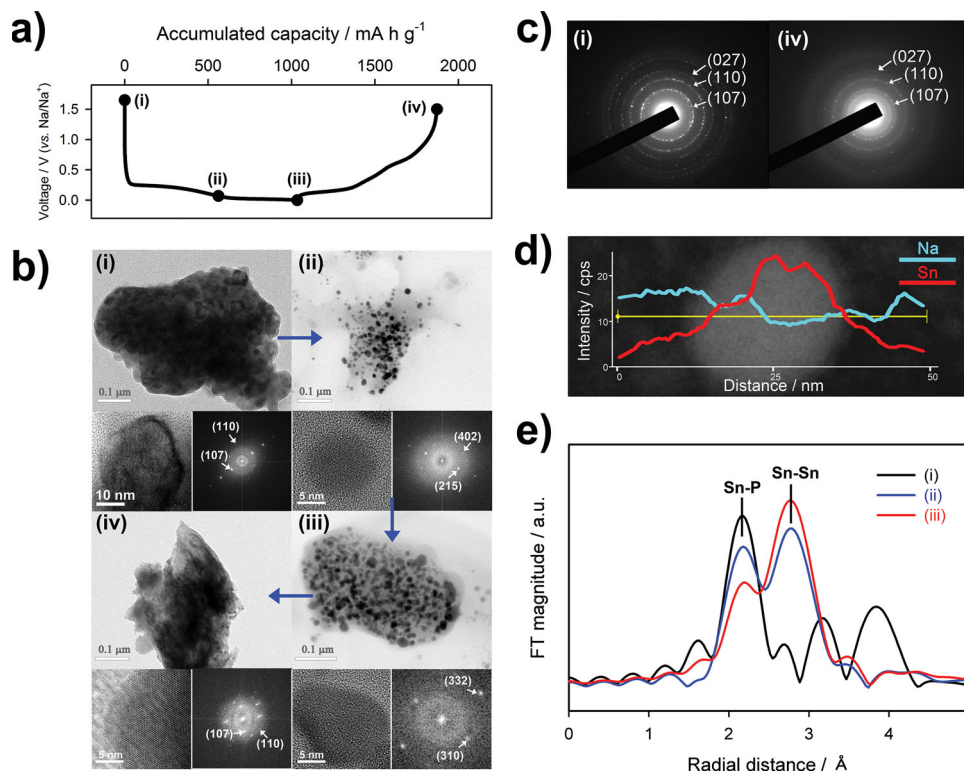
Figure 3. (a) First galvanostatic charge and discharge profiles of the Sn_4P_3 electrode obtained without an FEC additive. The different points indicate (i) pristine, (ii) 0.07 V, (iii) 0 V and (iv) 1.5 V. (b) The ex situ HR-TEM bright-field images at each point in (a) (insets of (i) through (iv): enlarged HR-TEM images (left) of crystalline regions and the corresponding FFT patterns (right)). (c) Electron diffraction (ED) patterns at the points (i) and (iv) in (a). (d) STEM dark-field image and EDX line profiles of Sn and Na in the nanocrystalline region at the point (ii) in (a). (e) Sn K-edge EXAFS spectra of Sn_4P_3 during sodiation.

Figure 5 shows a comparison of the voltage profiles of a phosphorus/carbon composite and Sn_4P_3. The redox potential of Sn_4P_3 is lower than that of phosphorus/carbon composites. This indicates that a full cell with higher energy density can be obtained using a Sn_4P_3 anode instead of a phosphorus anode, assuming that equal reversible capacities are utilized. The increase in the redox potential of cathode materials is limited owing to electrolyte decomposition at high potential, and thus it is important to decrease the redox potential of anode materials to increase the working voltage (energy density) of full cells. Therefore, Sn_4P_3 is an ideal anode material for Na-ion batteries. The thickness change in electrodes during sodiation and desodiation was measured through ex situ measurements of the electrode thickness (Figure 5). The cells were disassembled and the electrode thickness was measured manually at various points indicated in the corresponding voltage profile: (i) pristine, (ii) 0.07 V, (iii) 0 V, (iv) 0.5 V and (v) 1.5 V. After full sodiation until the redox potential of the working electrode reached 0 V vs. Na/Na⁺, the electrode thickness increased by 93%, which is lower than that in the previously reported case of the phosphorus/carbon composite (187%).[18] The electrode thickness change during sodiation and desodiation was reversible, and the initial electrode thickness was almost recovered with an expansion of only 11% after full desodiation until the redox potential of the working electrode reached 1.5 V vs. Na/Na⁺. The large volume change in Sn_4P_3 is a practical obstacle for its

commercialization, because the maximum acceptable degree of volume change for commercial electrodes is ~30%. Therefore, it is required to consider new approaches to alleviate cell deformation, including control of electrode porosity and the use of functional binders.

In conclusion, tin phosphide (Sn_4P_3) was obtained through ball milling, and we demonstrated, for the first time, its electrochemical performance as an anode material for Na-ion batteries. Sn_4P_3 is notable as a promising anode candidate for Na-ion batteries owing to its volumetric specific capacity, which is the highest among Na-ion insertion materials reported to date, and good electrical conductivity. In this study, Sn_4P_3 showed excellent electrochemical performance including (i) a reversible capacity of 718 mA h g⁻¹; (ii) very stable cycle performance with negligible capacity fading over 100 cycles; and (iii) an appropriately low redox potential of about 0.3 V vs. Na/Na⁺, which is ideal for an anode to achieve full cells with high energy density. The better cycle performance of Sn_4P_3 than Sn was attributed to the confinement effect of Sn nanocrystallites in the amorphous phosphorus matrix during cycling. In addition, the reversible sodiation/desodiation mechanism of Sn_4P_3 was revealed through ex situ TEM, EXAFS and XRD analyses. Finally, owing to the simple synthesis and excellent electrochemical performance of the Sn_4P_3, it is expected that various phosphide-based anode materials including Sn_4P_3 will be extensively studied for Na-ion batteries.
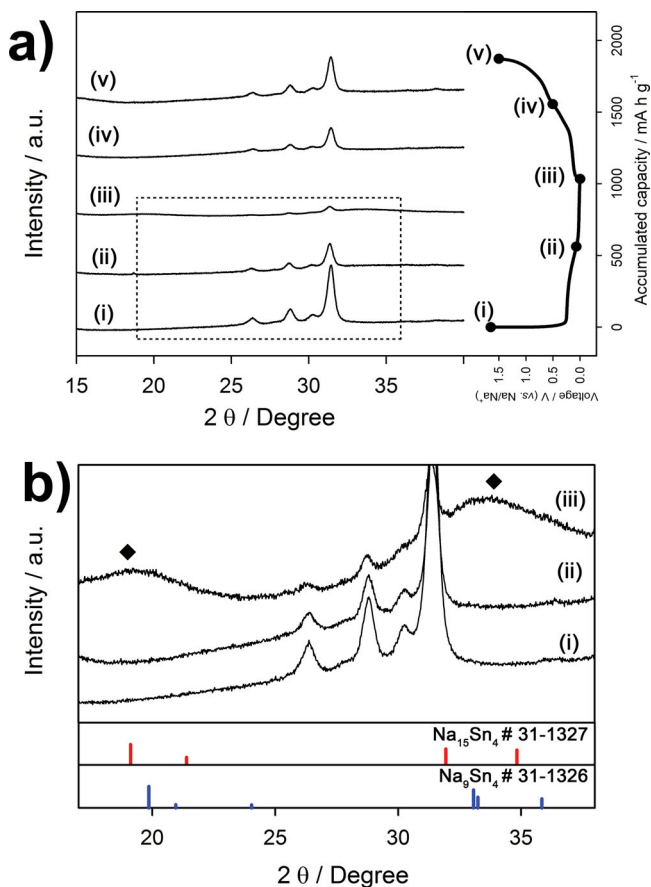
a)

b)

Figure 4. (a) Ex situ XRD patterns of the Sn_4P_3 electrode collected at various points as indicated in the corresponding voltage profile: (i) pristine, (ii) 0.07 V, (iii) 0 V, (iv) 0.5 V and (v) 1.5 V. (b) Enlarged ex situ XRD patterns during sodiation.

Experimental Section

Material Synthesis: Sn_4P_3 powder was prepared via mechanical ball milling using Sn (Aldrich, ≥ 99%) and red phosphorus powders (Aldrich, ≥99.99%). The molar ratio of Sn and P powders was 4:3. High energy mechanical ball milling (SPEX-8000) was carried out under an Ar atmosphere for an hour.
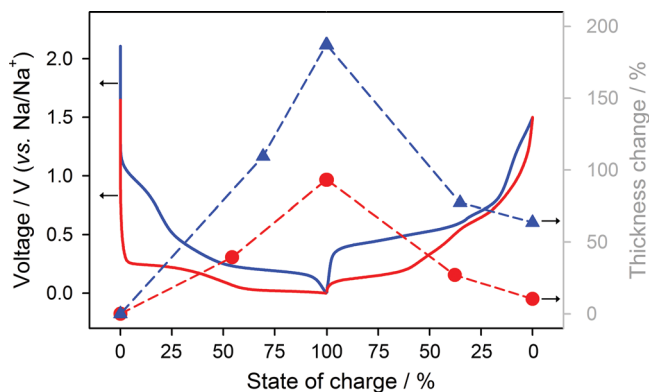
Figure 5. Voltage profiles of Sn_4P_3 (red line) and P/C composite (blue line) and the corresponding electrode thickness change during sodiation and desodiation (red circle: Sn_4P_3, blue triangle: P/C).

Material Characterization: Powder X-Ray diffraction (XRD) data were collected on a Rigaku D/MAX2500V/PC powder diffractometer using Cu-Kα radiation (λ = 1.5405 Å) operated in the 2θ range of 10–80°. SEM samples were examined using a JEOL JSM-6700F field-emission scanning electron microscope (FE-SEM). High-resolution TEM samples were investigated using a scanning transmission electron microscope (HR-TEM, STEM, JEOL JEM-2100F). Extended X-ray absorption fine structure (EXAFS) data were obtained at the Pohang light source (PLS beam line 7D) with a ring current of 270 mA at 3 GeV. Data were collected in a transmission mode using gas-filled ionization chambers as detectors.

Electrochemical Characterization: Samples of active materials were mixed with carbon black (Super P) and polyacrylic acid (PAA) in a 7:1:2 weight ratio. The slurry was cast onto current collector (Cu). The electrodes were dried at 120 °C in a vacuum oven overnight. Their electrochemical characteristics were evaluated using 2032 coin cells with a Na metal anode and 1 M NaClO$_4$ (Aldrich, ≥ 98%) in an ethylene carbonate and diethyl carbonate (1:1 v/v, PANAX ETEC Co., Ltd., Korea) electrolyte solution to which 5 wt.% fluoroethylene carbonate (FEC, Soulbrain Co. Ltd.) was added. A microporous polyolefin film was used as a separator. Galvanostatic experiments were carried out between 0.0 and 1.5 V (vs. Na/Na$^+$) at a current density of 100 mA g^{-1} by using WBCS 3000 (WonATech, Korea) under room temperature. The galvanostatic intermittent titration technique (GITT) was performed between 0 and 1.5 V (vs. Na/Na$^+$). A current pulse was applied for 30 min to measure the closed-circuit-voltage (CCV) and turned off for 1 h to obtain the quasi-open-circuit voltage (QOCV).

Supporting Information

Supporting Information is available from the Wiley Online Library or from the author.

Acknowledgements

[1] B. L. Ellis, L. F. Nazar, *Curr. Opin. Solid State Mater. Sci.* **2012**, *16*, 168.

[2] V. Palomares, P. Serras, I. Villaluenga, K. B. Hueso, J. Carretero-Gonzalez, T. Rojo, *Energ. Environ. Sci.* **2012**, *5*, 5884.

[3] V. Palomares, M. Casas-Cabanas, E. Castillo-Martinez, M. H. Han, T. Rojo, *Energ. Environ. Sci.* **2013**, *6*, 2312.

[4] H. Pan, Y.-S. Hu, L. Chen, *Energ. Environ. Sci.* **2013**, *6*, 2338.

[5] M. D. Slater, D. Kim, E. Lee, C. S. Johnson, *Adv. Funct. Mater.* **2013**, *23*, 947.

[6] S. Y. Hong, Y. Kim, Y. Park, A. Choi, N. S. Choi, K. T. Lee, *Energ. Environ. Sci.* **2013**, *6*, 2067.

[7] A. Darwiche, M. T. Sougrati, B. Fraisse, L. Stievano, L. Monconduit, *Electrochem. Commun.* **2013**, *32*, 18.

[8] Y. Xu, Y. Zhu, Y. Liu, C. Wang, *Adv. Energy Mater.* **2013**, *3*, 128.

[9] H. Zhu, Z. Jia, Y. Chen, N. Weadock, J. Wan, O. Vaaland, X. Han, T. Li, L. Hu, *Nano Lett.* **2013**, *13*, 3093.

[10] L. D. Ellis, T. D. Hatchard, M. N. Obrovac, *J. Electrochem. Soc.* **2012**, *159*, A1801.

[11] S. Komaba, Y. Matsuura, T. Ishikawa, N. Yabuuchi, W. Murata, S. Kuze, *Electrochem. Commun.* **2012**, *21*, 65.

[12] A. Darwiche, C. Marino, M. T. Sougrati, B. Fraisse, L. Stievano, L. Monconduit, *J. Am. Chem. Soc.* **2012**, *134*, 20805.

[13] J. Qian, Y. Chen, L. Wu, Y. Cao, X. Ai, H. Yang, *Chem. Commun.* **2012**, *48*, 7070.

[14] X. Zhou, Z. Dai, J. Bao, Y.-G. Guo, *J. Mater. Chem. A* **2013**.

[15] N. Yabuuchi, M. Kajiyama, J. Iwatate, H. Nishikawa, S. Hitomi, R. Okuyama, R. Usui, Y. Yamada, S. Komaba, *Nat. Mater.* **2012**, *11*, 512.

[16] L. Xiao, Y. Cao, J. Xiao, W. Wang, L. Kovarik, Z. Nie, J. Liu, *Chem. Commun.* **2012**, *48*, 3321.

[17] L. Ji, M. Gu, Y. Shao, X. Li, M. H. Engelhard, B. W. Arey, W. Wang, Z. Nie, J. Xiao, C. Wang, J.-G. Zhang, J. Liu, *Adv. Mater.* **2014**, n/a.

[18] Y. Kim, Y. Park, A. Choi, N.-S. Choi, J. Kim, J. Lee, J. H. Ryu, S. M. Oh, K. T. Lee, *Adv. Mater.* **2013**, *25*, 3045.

[19] J. Qian, X. Wu, Y. Cao, X. Ai, H. Yang, *Angew. Chem., Int. Ed.* **2013**, *52*, 4633.

[20] Y.-U. Kim, C. K. Lee, H.-J. Sohn, T. Kang, *J. Electrochem. Soc.* **2004**, *151*, A933.

[21] B. León, J. I. Corredor, J. L. Tirado, C. Pérez-Vicente, *J. Electrochem. Soc.* **2006**, *153*, A1829.

[22] V. Pralong, D. C. S. Souza, K. T. Leung, L. F. Nazar, *Electrochem. Commun.* **2002**, *4*, 516.

[23] D. C. S. Souza, V. Pralong, A. J. Jacobson, L. F. Nazar, *Science* **2002**, *296*, 2012.

[24] M. P. Bichat, T. Politova, J. L. Pascal, F. Favier, L. Monconduit, *J. Electrochem. Soc.* **2004**, *151*, A2074.

[25] F. Gillot, S. Boyanov, L. Dupont, M. L. Doublet, M. Morcrette, L. Monconduit, J. M. Tarascon, *Chem. Mater.* **2005**, *17*, 6327.

[26] S. Boyanov, J. Bernardi, F. Gillot, L. Dupont, M. Womes, J. M. Tarascon, L. Monconduit, M. L. Doublet, *Chem. Mater.* **2006**, *18*, 3531.

[27] Y. Kim, H. Hwang, C. S. Yoon, M. G. Kim, J. Cho, *Adv. Mater.* **2007**, *19*, 92.

[28] S. Boyanov, D. Zitoun, M. Ménétrier, J. C. Jumas, M. Womes, L. Monconduit, *J. Phys. Chem. C* **2009**, *113*, 21441.

[29] Y. Lu, J.-P. Tu, Q.-Q. Xiong, J.-Y. Xiang, Y.-J. Mai, J. Zhang, Y.-Q. Qiao, X.-L. Wang, C.-D. Gu, S. X. Mao, *Adv. Funct. Mater.* **2012**, *22*, 3927.

[30] J. Y. Jang, G. Park, S.-M. Lee, N.-S. Choi, *Electrochem. Commun.* **2013**, *35*, 72.

[31] M. C. Stan, R. Klöpsch, A. Bhaskar, J. Li, S. Passerini, M. Winter, *Adv. Energy Mater.* **2013**, *3*, 231.